Nature of Stable Single Atom Pt Catalysts Dispersed on Anatase TiO_2

Ho Viet Thang, Gianfranco Pacchioni[1]

Departimento di Scienza dei Materiali, Università di Milano-Bicocca, via Cozzi 55, 20125 Milano, Italy

Leo DeRita, Phillip Christopher

Department of Chemical Engineering, University of California, Santa Barbara, USA

Version 15.08.2018

Pt single atom catalysts anchored on the surface of anatase TiO_2 have recently been shown to be stable through oxidation and reduction conditions and exhibit higher catalytic activity in CO oxidation than Pt metallic clusters. In this work we unravel the atomistic nature of the isolated Pt_{iso} species on anatase TiO_2 thanks to the combination of CO probe molecule Fourier Transform Infrared (FTIR) and temperature programmed desorption (TPD) experiments with an extensive set of Density Functional Theory (DFT) calculations. We used the stretching frequencies and adsorption energies of CO bound to Pt as a fingerprint of the specific structure of the stable Pt_{iso} species. These consist of Pt atoms bound to two excess O atoms on the surface (PtO_2). The excess oxygen atoms on the surface arise from the formation of surface hydroxyl groups, and provide a solid anchor to the oxide support, which explains the high thermal stability of the single-atom Pt catalyst through oxidative and reductive treatments. Beside the single atom Pt species, also models of metallic, Pt_{metal}, and oxidized, Pt_{ox}, sub-nanometer clusters have been considered. Comparisons between characteristics of Pt_{iso} species and sub-nanometer Pt_{metal} and Pt_{ox} clusters demonstrate that the combination of CO vibrational frequency and adsorption energy can be an effective approach to differentiate these species.

Keywords:

Singe-atom catalyst; IR spectroscopy; TPD measurements; DFT calculations; TiO_2 anatase

[1] Corresponding author: Gianfranco.pacchioni@unimib.it

1. Introduction

Heterogeneous catalysts based on highly dispersed precious metal clusters are traditionally used in chemical conversion, and environmental remediation [1,2,3,4], thanks to the enhanced activity of small metal aggregates supported on thermally stable metal oxides. In some cases, the activity of transition metal clusters is inversely proportional to the size [5,6]. Therefore, reducing the size of the aggregates to form small but thermally stable active units is becoming a key strategy to produce more efficient metal catalysts, with the additional benefit of reducing the costs of materials. Ideally, the desired ultimate size is that of a single atom. However, these species usually tend to aggregate during the synthesis process, or in the course of the catalytic reaction due to low barrier diffusion processes [7]. High thermal stability of the single atom catalysts is thus a key factor to maximize the utilization and productivity of precious metals. Among these catalysts, Pt is preferentially used, as it is very active in CO oxidation [8,9], methanol oxidation [10], hydrogenation of styrene [11], automotive oxidation catalysts [12], dye-sensitized solar cells [13,14], etc. This has motivated an increasing interest of the scientific community to the field of single-atom catalysts in recent years. For example, thermally stable, atomically dispersed Pt on CeO_2 [15] or on Al_2O_3 [16] have been successfully synthesized by atom-trapping and sol-gel approaches. The highly thermal stability of the single Pt atoms is due to the strong interaction of Pt with a planar four-oxygen pocket on the CeO_2 surface [17] or to the under-coordinated Al^{3+} cations in Al_2O_3 [18]. Another promising strategy for stabilizing single Pt atoms is the modification of activated carbon by small phosphomolybdic acid clusters, in which the Pt atom was trapped on a four oxygen hollow site in planar geometry [19]. Therefore, the high stability of isolated Pt single atoms depends on the nature of support, the presence of defects on the substrates, or of under-coordinated cations, anions or other active ligands.

Recently, we reported an approach that successfully produced catalysts consisting of thermally stable Pt atoms grafted on 5 nm particles of anatase TiO_2, denoted as isolated Pt, Pt_{iso}, as also used here [20]. It was shown that the Pt_{iso} species remained as single atoms in a cationic charge state through thermal treatments in oxidative (450 °C in O_2) and reductive (250 °C) pre-treatments. Based on the results from scanning transmission electron microscopy (STEM) and Fourier transform infrared spectroscopy (FTIR) of adsorbed CO, it was reported that these Pt_{iso}/TiO_2 catalysts have a sharp unchanged IR band for CO adsorption (2112 cm^{-1}) following calcination at 450 ^oC, and *in-situ* reduction at 250 °C. The sharpness of the CO stretch (full width at half maximum, FWHM of 6-8 cm^{-1}) indicated that the Pt_{iso} species likely resided in a common adsorption location on the support (ie. single site species). Broader bands associated with CO

adsorption on sub-nanometer diameter metallic Pt clusters, Pt_{metal} (2040-2090 cm^{-1}), and oxidized Pt clusters, Pt_{ox} (2090-2140 cm^{-1}) were also reported for higher weight loading Pt catalysts. The various supported species were classified also by using Temperature-Programmed Desorption (TPD) experiments which showed that the CO adsorption energy follows the trend $Pt_{iso} << Pt_{metal} < Pt_{ox}$ [20].

In an effort to better understand where the Pt_{iso} species is located and what its local structure looks like, a detailed analysis of the TPD-IR has been performed to produce more quantitative estimates of the CO adsorption properties and correlated with a theoretical investigation. Single Pt atoms, PtO, and PtO_2 units, small Pt_3 and Pt_4 nano clusters, and small oxidized Pt_xO_y clusters deposited on regular and stepped anatase TiO_2 surfaces have been studied by using the PBE+U method. Other models considered consist of a Pt atom replacing a lattice Ti or a lattice O on the surface. The CO molecule was used to probe the location, nature and bonding capability of the Pt atoms or Pt clusters under reducing or oxidizing conditions. The sensitivity of the CO molecule, in terms of vibrational frequency and adsorption energy, to the changes in Pt oxidation states and the local environment, provides an excellent probe to check the nature of the catalyst. The use of both CO vibrational frequency and adsorption energy for differentiating Pt location and structure is critical as it has been shown that the vibrational frequency of adsorbed CO alone is not sufficient to unambiguously identify the state of Pt species [21].

There are few examples where the exact nature of the single-atom catalysts has been unambiguously proven. For example, in a recent study, based on a comparison of FTIR and TPD spectra, TEM images, and DFT calculations, the nature of highly dispersed, thermally stable Ru species on monoclinic zirconia, m-ZrO_2, has been elucidated [22]. One of the active species on the surface of the catalyst consists of isolated Ru atoms bound to an O atom of the surface derived from a hydroxyl group. This leads to the formation of a RuO species with low mobility and strong capacity to bind CO and other molecular species as well [22].

In this report, we conclude from the DFT calculated structures that the high thermal stability of single Pt atoms results from PtO_2 units strongly bound on the TiO_2 surface, which shows excellent agreement with the calculated adsorption energy and vibrational frequency of CO from the experimental measurements by TPD-IR. It is demonstrated that the proposed Pt_{iso} species can be differentiated from other Pt_{iso} adsorption geometries and sub-nanometer oxidized and reduced Pt clusters based on the characteristics of CO adsorption. The paper is organized as follows. In Section 2 we describe the experimental and computational procedures used. Section 3, Results and Discussion, has been divided in sub-sections. First we report the experimental IR and TPD data with

the measured CO adsorption properties (3.1). In Section 3.2 we report the results of the DFT calculations analyzing the various models of Pt catalysts considered. The conclusions are summarized in Section 4.

2. Experimental and Computational Methods

2.1 Experimental methods

The synthesis of catalysts containing exclusively Pt_{iso} species was achieved as previously described, which utilized low weight loadings of Pt coupled with highly basic solution conditions to promote high dispersion, stemming from strong electrostatic adsorption of cationic Pt precursors to the support [20]. For the synthesis of Pt catalysts containing nanometer sized Pt clusters and no Pt_{iso} species, an incipient wetness (dry) impregnation (DI) procedure was used at 1% Pt weight loading as previously described [20]. All catalysts were calcined in a tube furnace at 450 °C for 4 hours in flowing air to ensure removal of all amine and nitrate ligands from the $Pt(NH_3)_4(NO_3)_2$ precursor.

Following calcination, catalysts were loaded into a Harrick Low Temperature Reaction chamber for the Pt_{iso} catalyst characterization, or a Harrick High Temperature Reaction chamber for the Pt_{metal} and Pt_{ox} characterization. A Thermo Scientific Nicolet iS10 FTIR spectrometer with mercury cadmium telluride (MCT) detector cooled by liquid nitrogen was used. All gases fed to the reactor were regulated by mass flow controllers and passed across an isopropyl alcohol-liquid nitrogen cold trap held at -75 °C and a quartz tube filled with Drierite desiccant to remove moisture. The temperature of the reactor bed was calibrated for both reactors to ensure accurate measurements during temperature programmed desorption experiments.

Once loaded into the reactor and prior to collecting spectra, catalysts were pretreated by either *in-situ* oxidation (300 °C for 30 min in 50 sccm of 10% O_2/Ar) for the Pt_{ox} catalyst or by *in-situ* reduction (250 °C for 1 h in 50 sccm of 10% H_2/Ar) for the Pt_{iso} and Pt_{metal} catalysts. The Pt_{metal} and Pt_{ox} catalysts were then cooled in Ar to room temperature. Due to the relatively low stability of CO on Pt_{iso} at room temperature, the reaction chamber was evacuated to -85 kPa and cooled by liquid nitrogen to -140 °C. Background spectra were collected once desired temperatures were reached, CO was passed over the catalysts to saturation and the cell was then flushed with Ar.

TPD experiments were performed using a relatively slow ramp rate, β= 10 °C/min, which enabled collection of high quality FTIR spectra at closely spaced temperatures. Redhead Analysis was performed by tracking the change in normalized, integrated intensity of the CO stretches at the

various Pt adsorption sites as a function of temperature. A numerical derivative of the change in intensity as a function of temperature was then taken. The local maxima of the numerical derivative is a measure of the rate at which CO desorption is highest and corresponds to the temperature of peak desorption, T_p. With an assumed rate constant of $\nu=10^{15}$ s^{-1} previously justified [23,24] and using the ramp rate β= 10 °C/min, an adsorption energy for CO was calculated using the Redhead Equation [25], Equation 1 below.

$$\frac{E}{RT_p} = \ln\left(\frac{\nu T_p}{\beta}\right) - 3.64 \qquad (1)$$

2.2 Computational methods

The calculations were performed using the Vienna Ab-initio Simulation Package (VASP) [26] with Perdew-Burke-Ernzerhof (PBE) generalized gradient approximation (GGA) exchange-correlation functional [27]. The self-interaction problem in DFT has been partly corrected using the DFT+U approach where the Hubbard's U parameter is empirically set to 3 eV [28] for Ti 3d states. The Projector Augmented Wave (PAW) [29,30] method was adopted to treat core electron and nuclear interaction. The valence electrons explicitly treated are: Ti($3p^6$, $3d^4$, $4s^2$), Pt ($5p^6$, $5d^9$, $6s^1$), O ($2s^2$, $2p^6$) and C ($2s^2$, $2p^4$). We used plane wave basis set with cutoff energy of 400 eV and the calculation was done at the gamma point. The optimized structure was relaxed when the forces are <0.01 eV/A^2 and the electron threshold is less than -0.002 eV.

3x1 and 2x1 supercell slab of five-atomic layers were used to model the anatase TiO_2 (101) and the stepped TiO_2 (145) surfaces, respectively. This corresponds to the formulas of $Ti_{60}O_{120}$ and $Ti_{88}O_{176}$. The slabs are separated by more than 15 Å of vacuum to avoid the interaction between them. The detailed description of these models is given in Ref. 31. The TiO_2 (101) surface terminates with two types of Ti cation, 5-fold coordinated Ti (Ti_{5c}) and 6-fold coordinated Ti (T_{6c}), located lower than Ti_{5c}, and two types of O anion, 2-fold coordinated O sites (O_{2c}) and 3-fold coordinated O sites (O_{3c}), Figure S1.

The CO adsorption energies, in eV, were calculated as the difference between isolated species and the adsorption complexes. Positive values indicate stable adsorbed species. The CO frequencies were computed within the harmonic approximation, in which CO and its first neighboring atoms were considered in the calculation. In gas phase, the CO bond length (1.144 Å) and stretching frequency (2125 cm^{-1}) are obtained at the PBE level. A scaling factor α = 2143/2125 = 1.0085 has been applied to all frequencies to take into account the difference with respect to the

experimental CO frequency (2143 cm^{-1}). The effective charge of Pt atoms was evaluated by using Bader approach which is proposed by Henkelman et al. [32,33,34,35].

3. Results and Discussion

3.1 CO adsorption energies and their relation to vibrational frequencies

Figure 1 shows IR measurements of adsorbed CO on isolated Pt atoms, Pt_{iso}, 1 nm metallic Pt clusters (Pt_{metal}), and 1 nm pre-oxidized Pt clusters (Pt_{ox}) at various temperatures during TPD experiments. Figure 1A shows IR spectra of CO adsorbed to Pt_{iso} following the mild reduction pretreatment. A single CO stretch was observed at 2113 cm^{-1} consistent with previously assignments of CO adsorption to cationic Pt_{iso} species [36,37, 15,20]. As before, a narrow FWHM of 10.5 cm^{-1} was observed and during the TPD, total desorption of CO was observed by ~5 °C. Due to the high degree of symmetry and unchanging band position, the band was approximated well by both a Gaussian and Lorentzian (Cauchy) functions. The peak area was quantified using the FWHM, CO band position, and normalized intensity (height) at each temperature to determine T_p, which for the single CO adsorption site was found to be -10 °C using both fitting functions, corresponding to a calculated adsorption energy of 0.87 eV.

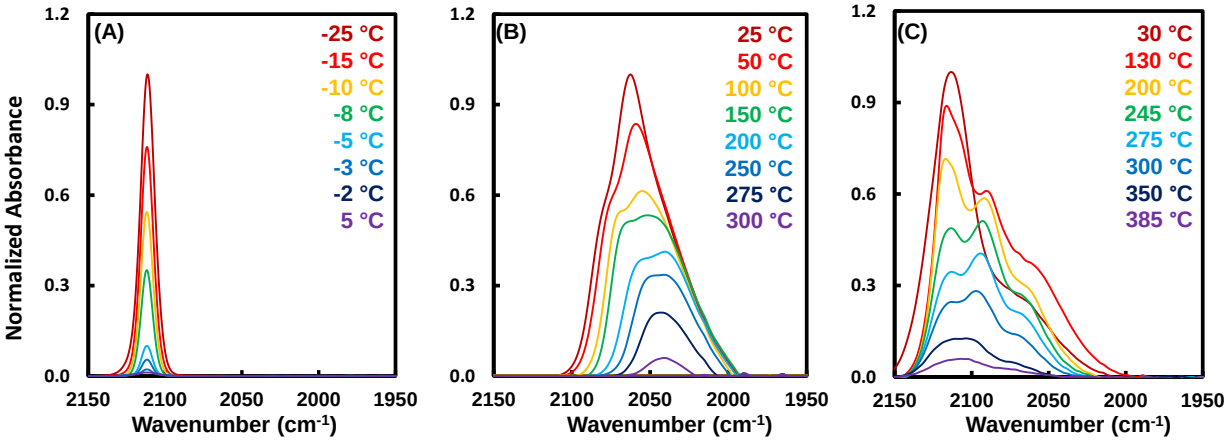

Figure 1. CO TPD-IR spectra from Pt_{iso}, Pt_{metal} and Pt_{ox} catalysts. (A) CO TPD-IR spectra taken from a reduced 0.025% Pt_{iso}/TiO_2 catalyst after CO saturation at -140 °C and Ar flush. (B) CO TPD-IR spectra following room temperature adsorption to saturation coverage and flushing in He on a pre-reduced 1 wt % Pt/TiO_2 catalyst. (C) CO TPD-IR spectra during an identical TPD experiment on a pre-oxidized 1 wt % Pt/TiO_2 catalyst as shown in (B).

Redhead analysis of the 1 wt% Pt clusters was less straightforward than the case of Pt_{iso} where there was a single well-defined CO stretch. For Pt_{metal}, four Gaussian functions (fitting using Lorientzian functions gave similar results) of equal FWHM (20 cm^{-1}) were used to approximate each spectrum and the remaining parameters of the Gaussian (band center and height) were varied

manually until the fit was sufficiently accurate, see Figure S2A. To aid in fitting, constraints were imposed on the manual fitting. First, because it is well known that dipole-dipole coupling blue shifts the band position of CO on metals [38], the CO stretching frequency of each Gaussian function fit was either held constant from the previous spectrum or decreased during the temperature ramp. Second, the height of a peak was only ever increased if a higher frequency CO-Pt stretch had decreased suggesting that desorption induced minor restructuring or that CO had diffused to a lower coordinated Pt site, known to bind CO more strongly [39]. Similar to our previous studies, no evidence of energy transfer between lower and higher frequency CO stretches was observed during the CO adsorption or desorption, which is well known on stepped Pt single crystals [40,41,42]. This suggests the large radius of curvature on these small Pt clusters minimized coupling between CO dipoles on sites with different coordination.

Once all spectra were fit, a numerical derivative of the area of each CO stretch was taken to find local peak desorption temperatures. In the case of fitting multiple peaks it proved more useful to look at the derivative of the cumulative desorption profile to identify the peak desorption temperatures: 75, 180, 265, and 300 °C corresponding to bands at 2079, 2062, 2045 and 2028 cm^{-1}, respectively. The cumulative desorption profile was then subdivided and the derivative of the sum of the two higher frequency Gaussian fits and of the two lower frequency Gaussian fits were used to assign the CO adsorption sites to the T_p values as shown in Figure S3(A). Because IR spectra take time to collect and the ramp rates should be relatively fast for TPD experiments where Redhead analysis is applied, the data spacing is larger than desired and the derivatives sometime span large temperature ranges. For this reason, a minimum threshold for the numerical derivative, $dA/dT > 0.1$, was used to filter out minor fluctuations in the derivative which should not be considered peak desorption temperatures. In Figure S3(A) the derivative of the summed higher coordination CO-Pt stretches have 2 clear local desorption maxima at 75 and 180 °C which are most reasonably assigned to CO desorption from the most highly coordinated Pt in the metal clusters, respectively, 2079 and 2062 cm^{-1} [40,43,44]. For the lower coordination fit local desorption maxima at 265 and 300 °C were assigned to 2045 and 2028 cm^{-1} respectively [39,40,43,44].

A similar analysis of CO desorption from Pt_{ox} sites was executed. Due to the additional presence of CO stretches associated with adsorption on cationic Pt sites, six Gaussian functions, rather than four as for CO on Pt_{metal}, were used to fit the spectra (FWHM = 20 cm^{-1}). The following CO band positions were observed: 2117, 2103 cm^{-1} (CO stretches associated with adsorption on cationic Pt) [45] and 2085, 2066, 2049, 2031 cm^{-1} (CO stretches associated with adsorption on metallic Pt sites), Figure S3(B). We note that CO exposure to the pre-oxidized Pt clusters likely

induced partial reduction causing the co-existence of CO adsorption to cationic and metallic Pt atoms. Numerical derivatives were again taken for the identified stretches tracked in the fitting. Directly correlating the CO-Pt stretches to the peak desorption temperatures proved difficult due to the multitude of ways six peaks can approximate a spectrum accurately. Since the Pt_{ox} stretches were of particular interest, it made sense to group the areas into generalized CO on cationic and metallic Pt cumulative areas and perform the derivative analysis as shown in Figure S3(B). In Figure S3(B) there are three obvious CO peak desorption temperatures (50, 150, and 270 °C) which correspond to the three identified metallic Pt-CO stretches. There are also 3 higher peak desorption temperatures for the CO stretches associated with adsorption on cationic Pt sites at 240, 300, and 350 °C which are assigned to 2115, 2110, and 2105 cm^{-1}. While only two stretches associated with CO adsorbed on cationic Pt were initially identified during the fitting, an intermediate stretch around 2110 cm^{-1} was masked by the overlap of the other cationic Pt-CO stretches. A summary of the identified vibrational CO-Pt stretches and their corresponding adsorption energies obtained through Redhead analysis (see Equation 1) is tabulated in Table 1 below.

Table 1. Summary of Adsorption Energies of CO to Pt_{iso}, Pt_{metal}, and Pt_{ox} Calculated Using Redhead Analysis

Material	Pt site description	Band center (cm^{-1})	$\Delta\nu$ (cm^{-1})	Tp (°C)	E_{ads} (eV)
0.025% Pt/TiO_2 250 °C reduction	Pt single site	2113	-30	-10	0.87
1% Pt/TiO_2 250 °C reduction	Higher coordination metallic Pt	2079	-64	75	1.16
		2062	-81	80	1.51
	Lower coordination metallic Pt	2045	-98	265	1.81
		2028	-115	300	1.93
1% Pt/TiO_2 300 °C oxidation	Cationic Pt	2117	-26	240	1.72
		2110	-33	300	1.93
		2105	-38	350	2.10
	Metallic Pt	2086	-57	50	1.07

	2070	-73	150	1.41
	2056	-87	270	1.82

From the values presented in Table 1, a relationship between the adsorption energy and the vibrational frequency of each corresponding CO stretch was plotted, Figure 2. A linear relationship between the vibrational frequency of CO and the adsorption energy is observed over the range of metallic Pt adsorption sites for both the fully reduced Pt_{metal} catalyst and the partially reduced Pt_{ox} catalyst. From the slope, it can be seen that for every 10 cm^{-1} decrease in the vibrational frequency of a CO-Pt stretch, there is an increase in adsorption strength of 0.15 eV for metallic Pt adsorption sites. Though there are too few data points to relate adsorption energies to cationic Pt adsorption sites, there is a similar trend with lower frequency CO stretches having higher CO adsorption energy. The CO stretching frequency has previously been linearly related to the Pt coordination number for metallic Pt sites independent of the support [8].

This analysis demonstrates that the Pt coordination number has a direct influence on the CO adsorption energy and vibrational frequency [8]. Likely, low coordination Pt adsorption sites bind CO more strongly due to greater back-bonding from the Pt d orbital and higher electron density in the atom, while high coordination adsorption sites exhibit less back-bonding due to distribution of electron density across neighboring Pt atoms. A similar argument holds true for relationships between CO vibrational frequency and metallic Pt coordination number. This relationship between Pt coordination number and CO adsorption energy seems to also hold true for the cationic Pt sites, but in this case due to the coordination with highly electronegative oxygen, the electron density of the Pt atom adsorbing CO will be significantly decreased causing the significant blueshift in the vibrational frequency. Interestingly, it may be expected that the cationic Pt sites should inherently bind CO more weakly than metallic Pt sites based on the nature of the bond, however it is also important to consider the local coordination number and environment for each adsorption site.

The adsorption energy of CO to the three catalyst materials quantitatively correlated with previously qualitative observations: Pt_{ox} has higher CO adsorption energies (1.72-2.10 eV) than Pt_{metal} (1.16-1.93), except at the lowest coordinated Pt sites (i.e. edges, corners) and both have much higher adsorption energy than Pt_{iso} (0.87 eV) [20]. The difference in adsorption energy between Pt_{iso} and Pt_{ox} despite similar stretching frequencies is a useful characterization tool to distinguish the sites given similarities in oxidation state and CO stretching frequency [46]. Furthermore, this suggests

that while the charge state of Pt atoms in Pt_{ox} clusters and Pt_{iso} may be similar, differences in their local coordination cause significant differences in the CO adsorption.

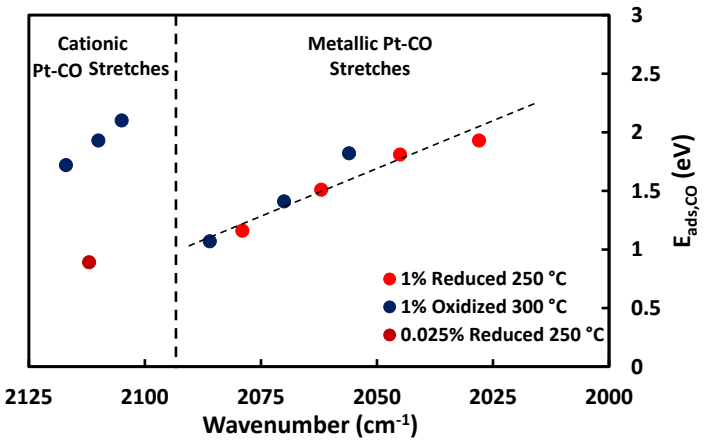

Figure 2. Adsorption energies of CO inferred from Redhead analysis as a function of vibrational frequency for the experiments shown in Figure 1.

3.2. Computational models of supported Pt species

To understand the experimental CO adsorption energies and vibrational frequencies shown for various sub-nanometer Pt species, extensive DFT calculations were performed on various forms of Pt_{iso} and small metallic and oxidized Pt clusters in the gas phase and on TiO_2 supports.

3.2.1 CO on gas-phase Pt, PtO and PtO_2 species

We first considered CO adsorption on free, gas-phase Pt atom, PtO and PtO_2 molecules, Table 2. This is useful to assess the basic properties of the CO-Pt bonding without any effect of the support. CO binds very strongly to a Pt atom in zero oxidation state, 3.79 eV, and gives rise to a large red-shift of the CO stretching frequency from the gas phase CO stretch, -74 cm^{-1}. On PtO CO forms a linear complex, Figure S4, the bond strength is reduced to 2.06 eV, but the red-shift is only partly reduced, being of -53 cm^{-1}, Table 2. Thus, despite a formal Pt oxidation state of +II, the CO frequency is red-shifted, and not blue-shifted, as one could expect due to the positive charge on the Pt atom (+0.51 $|e|$ according to the Bader analysis, see Table 2). The last case considered is that of CO bound to a PtO_2 molecule (see Figure S4). Here the bonding is very weak, 0.30 eV, but surprisingly the CO stretching frequency is red-shifted by more or less the same amount found for PtO (-55 cm^{-1}). Thus, even a +IV formal oxidation state of Pt as in PtO_2 results in a red-shift of the CO frequency from the gas phase CO stretch.

Table 2. Formal Pt oxidation state, adsorption energy (E_{ads}, eV), C-O bond length (R_{CO}, Å), C-Pt distance (R_{CPt}, Å), Bader charge of Pt (Q |e|), scaled harmonic CO stretching frequency (ω_e, cm^{-1}) and frequency shift with respect to the gas-phase (cm^{-1}) for CO adsorption on PtO_x gas-phase clusters.

System	CO site	E_{ads} (eV)	R_{CO} (Å)	R_{CPt} (Å)	Q (|e|)	ω_e (cm^{-1})	$\Delta\omega_e$ (cm^{-1})
Gas-phase species							
Pt	Pt^0	3.79	1.168	1.752	0.08	2069	-74
PtO	Pt^{II}	2.06	1.153	1.931	0.51	2090	-53
PtO_2	Pt^{IV}	0.30	1.158	1.836	1.10	2087	-55

3.2.2 Single Pt atoms, Pt_{iso} on a-TiO_2 (101) and stepped a-TiO_2 (145) surfaces

We adopted five models for the adsorption of a single Pt atom on the a-TiO_2 (101) surface, Figure 3. This includes a Pt atom, $(Pt)_{ads}$, a PtO unit, $(PtO)_{ads}$, a PtO_2 unit, $(PtO_2)_{ads}$, and a Pt atom substitutional to Ti, $(Pt)_{subTi}$, or to O, $(Pt)_{subO}$, in the lattice. Similar to our recent study [22], we assign formal oxidation states of 0, +I, +II, +IV and –II to Pt in $(Pt)_{ads}$, $(PtO)_{ads}$, $(PtO_2)_{ads}$, $(Pt)_{subTi}$, $(Pt)_{subO}$, respectively. We provide here a brief rational of these formal charges, making clear that all our computed systems are charge neutral. An adsorbed Pt atom, $(Pt)_{ads}$, has obviously formal charge 0. In the $(PtO)_{ads}$ unit Pt has a formal charge +I since the O atom is that of a previous OH group, and forms two bonds, one with a Ti atom of the surface, and one with the Pt atom. In the $(PtO_2)_{ads}$ unit the Pt atom is bound to two O atoms previously part of OH groups; thus the Pt atoms has a formal charge +II. Notice that for these reasons the formal charges of the $(PtO)_{ads}$ and $(PtO_2)_{ads}$ supported species are different from those of the same units in the gas-phase, see Table 2. If the Pt atom is replacing a Ti^{4+} cation we assign a formal charge +IV, while when it replaces an O anion of the surface it assumes a formal charge –II.

A Pt atom is stabilized by interaction with the oxygen atoms of the TiO_2 (101) surface. As reported in previous DFT studies [47,48], the atom can be adsorbed on three different sites with the most stable one corresponding to a bridging position between two O_{2c} atoms. We thus consider only this site, Figure 3a. The second and the third models, PtO and PtO_2, can be viewed as the result of the interaction of a Pt atom with one or two O atoms from OH groups on the surface. These can be

naturally present or can be introduced on purpose [20]. The extra oxygen atoms are considered to sit on the Ti_{5c} sites as these have higher activity than the Ti_{6c} sites. The most stable structures of $(PtO)_{ads}$ and $(PtO_2)_{ads}$ at the TiO_2(101) terraces are shown in Figure 3b and 3c, respectively. Notice that $(PtO_2)_{ads}$ has a particular structure where the Pt atom is coordinated to three O atoms, two from the former OH groups and one from the lattice, forming a particularly stable PtO_3 unit; here the Pt atom is directly above a Ti atom from the lattice, Figure 3c. In the last two models considered, the Pt atom replaces Ti or O at the lattice sites, Figure 3d and 3e, respectively. The same species have been considered also on a stepped TiO_2(145) surface, Figure 4.

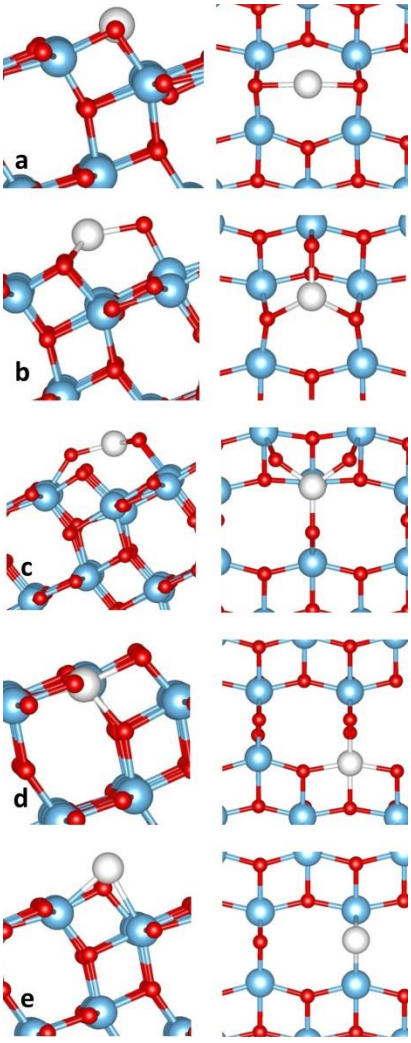

Figure 3. Pt atom adsorbed on a-TiO_2 (101) terrace: a) atomic Pt adsorption, b) PtO, c) PtO_2, d) substitution of Pt at Ti_{5c} site, e) substitution of Pt at O_{2c} site with side view (left) and top view (right). Ti, O and Pt are blue, red and white spheres, respectively.

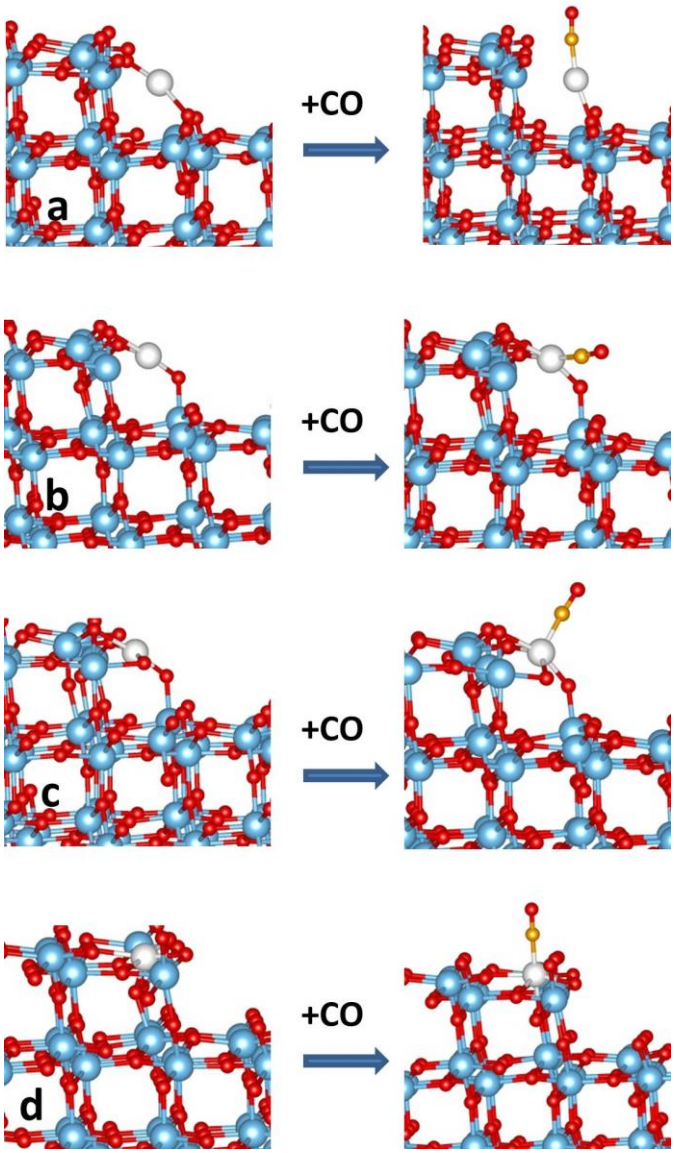

Figure 4. Pt atom adsorbed on a-TiO_2 (145) stepped surface and formation of a Pt-CO complex: a) atomic Pt adsorption, b) PtO, c) PtO_2, d) substitution of Pt at Ti_{5c} site. Ti, O and Pt are blue, red and white spheres, respectively.

We first considered a CO molecule adsorbed on a Ti_{5c} cation of the TiO_2(101) surface; here CO binds weakly (0.34 eV) and the CO stretching frequency, 2187 cm^{-1}, is blue-shifted by +44 cm^{-1} (Table 3) in good agreement with experimental measurements [31].

The results for CO adsorption on single Pt atoms in different configurations are collected in Table 3 (see also Figure S5). CO binds to an adsorbed Pt atom, $(Pt)_{ads}$, on TiO_2(101) with a very strong binding energy (2.96 eV) and large redshift (-79 cm^{-1}) with respect to free CO. Notice that the binding energy is reduced by about 1 eV compared to the free Pt atom, while the CO frequency shifts is almost the same, Table 2. There is a large charge transfer from the under-coordinated Pt atom to the anti-bonding $2\pi^*$ CO orbital resulting in an elongated CO bond length. The Bader

charge of Pt is nearly zero (+0.17 |e|). Very similar results are found for the stepped surface. Here CO binds to Pt by 2.74 eV, and $\Delta\omega_e$ is -71 cm^{-1}. Notice that this reflects the bond-order conservation principle: Pt_{ads} is more strongly bound on TiO_2 step (3.17 eV) than on TiO_2 terrace (2.75 eV); as a consequence, CO binds more strongly to a Pt atom bound at terrace than at a step, Table 3. We notice that $(Pt)_{ads}$ is moving with respect to the original position when CO is bound, Figure S5a.

Table 3. Formal Pt oxidation state, adsorption energy (E_{ads}, eV), C-O bond length (R_{CO}, Å), C-Pt distance (R_{CPt}, Å), Bader charge of Pt (Q |e|), scaled harmonic CO stretching frequency (ω_e, cm^{-1}) and frequency shift with respect to the gas-phase (cm^{-1}) for CO adsorption on Pt atom on a-TiO_2 (101) surface.

System	CO site	E_{ads} (eV)	R_{CO} (Å)	R_{CPt} (Å)	Q (|e|)	ω_e (cm^{-1})	$\Delta\omega_e$ (cm^{-1})
a-$(TiO_2)_{60}$[a]	Terrace	Ti^{IV}	0.34	1.138	2.467	-	2187	+44
$(Pt)_{ads}(TiO_2)_{60}$	Terrace	Pt^0	2.96	1.164	1.811	+0.17	2064	-79
$(Pt)_{ads}(TiO_2)_{88}$	Step	Pt^0	2.74	1.163	1.808	+0.08	2072	-71
$(PtO)_{ads}(TiO_2)_{60}$	Terrace	Pt^I	3.06	1.157	1.824	+0.88	2102	-41
$(PtO)_{ads}(TiO_2)_{88}$	Step	Pt^I	2.91	1.155	1.837	+0.82	2101	-42
$(PtO_2)_{ads}(TiO_2)_{60}$	Terrace	Pt^{II}	1.07	1.152	1.858	+1.19	2121	-22
$(PtO_2)_{ads}(TiO_2)_{88}$	Step	Pt^{II}	0.52	1.153	1.852	+1.32	2107	-36
$(Pt)_{subTi5c}(Ti_{59}O_{120})$	Terrace	Pt^{IV}	1.73	1.146	1.876	+1.48	2148	+5
$(Pt)_{subTi5c}(Ti_{87}O_{176})$	Step	Pt^{IV}	1.88	1.146	1.877	+1.43	2148	+5
$(Pt)_{subTi5c}(Ti_{87}O_{176})$	Step	Pt^{IV}	1.76	1.146	1.881	+1.43	2146	+3
$(Pt)_{subO2c}(Ti_{60}O_{119})$	Terrace	Pt^{-II}	1.14	1.161	1.899	-0.51	2029	-114
$(Pt)_{subO3c}(Ti_{60}O_{119})$	Terrace	Pt^{-II}	1.07	1.159	1.917	-0.62	2035	-108

[a] Ref. 31

On $(PtO)_{ads}$ Pt is in a positive oxidation state (Bader charge +0.88 |e|). The CO binding energy, 3.06 eV, is similar, to that of $(Pt)_{ads}$ (2.96 eV), but the red-shift in CO stretching frequency is smaller, -41 cm^{-1} vs. -79 cm^{-1}, Table 3. Upon CO binding, the $(PtO)_{ads}$ species is displaced from the original position, Figure S5b. The $(PtO)_{ads}$ species has been studied also on the TiO_2(145)

stepped surface, Figure 4. Notice that the PtO unit is more strongly bound to a TiO_2 step, 2.30 eV, than on a TiO_2 terrace, 1.59 eV. However, the CO adsorption properties are very similar to those found on the TiO_2 terrace: the CO binding energy to $(PtO)_{ads}$ (2.91 eV) is only 0.15 eV smaller and $\Delta\omega_e$(CO) is practically the same, -42 cm^{-1}, Table 3.

We consider now the $(PtO_2)_{ads}$ species supported on both terrace and step sites of the TiO_2 surface. These fragments are bound with respect to the free PtO_2 unit by 0.60 eV (terrace) and 1.06 eV (step). The charge on Pt is similar in the two cases, Table 3 (+1.2 |e| vs.+1.3 |e|). We have seen above that in the gas-phase CO binds very weakly to the PtO_2 complex (0.30 eV, Table 2), and that the CO $\Delta\omega_e$ is -55 cm^{-1}. Given these results, it is not surprising that CO adsorption on $(PtO_2)_{ads}/TiO_2$ is weaker than on the Pt_{ads} and $(PtO)_{ads}$ units discussed before. In particular, E_{ads}(CO) is 1.07 eV (terrace) and 0.52 eV (step), Table 3. The CO stretching frequencies, 2107-2121 cm^{-1}, are red-shifted by -22 cm^{-1} for $(PtO_2)_{ads}$ on a terrace, and by -36 cm^{-1} for the step case, Table 3. Both the absolute values and the shifts of the CO vibrational mode are very close to the experimental value for the Pt_{iso} species (2113 cm^{-1}, Table 1). Furthermore, the position of $(PtO_2)_{ads}$ after CO adsorption does not change much, indicating a structural stability of the complex. Experimentally, an adsorption energy of 0.87 eV has been deduced from the TPD spectra, Table 1; this is due to a single or highly homogeneous species (see the sharp IR signal, Figure 1A) [49]. Since the DFT+U approach tends to slightly over-bind, the 0.87 eV measured binding energy fits better with that computed for the $(PtO_2)_{ads}$ complex formed on the terraces of the TiO_2(101) surface (1.07 eV). Therefore, we tentatively assign the observed Pt_{iso} species to this structural motif.

The next case considered is that of a Pt atom replacing a lattice Ti. Here Pt has the highest formal oxidation number (+IV) and also the highest Bader charge, +1.4-1.5 |e|, Table 3. We also substituted Pt at a Ti_{6c} sites on both terrace and steps, but the CO adsorption results in the formation of CO_2 by interaction with a lattice oxygen, reflecting the high instability of the incorporated $(Pt)_{subTi6c}$ atom. CO binds to $(Pt)_{subTi5c}$ with an adsorption energy of 1.73 eV (terrace) and 1.88 eV (step), and gives rise to a small blue-shift of the CO stretching frequency of +5 cm^{-1} on both terraces and steps, Table 3. Clearly, a Pt atom substitutional to Ti_{5c} is not a good model for the Pt_{iso} species observed experimentally.

The last cases considered are those of CO adsorbed to a Pt atom sitting on an oxygen vacancy (i.e at a lattice O position). Previous studies of Pt atom adsorption on rutile TiO_2 have shown that Pt is strongly trapped at oxygen vacancy sites [50]. Thus, two sites, O_{3c} and O_{2c} were investigated (only on TiO_2 terraces). A negative charge on Pt is found for both $(Pt)_{subO}$ species

(Bader charges from -0.5 |e| to -0.6 |e|). This results in very large red-shift in CO stretching frequencies, of about -110 cm^{-1}, Table 3. The CO adsorption energies are slightly above 1 eV, Table 1. Also in this case, the results are not compatible with the observed features for the Pt_{iso} species.

3.2.3 Metallic Pt clusters, Pt_{metal}, on a-TiO_2 (101) surface

Two clusters, Pt_3 and Pt_4, have been considered to model metallic Pt nanoparticles, Pt_{metal}, deposited on the a-TiO_2 (101) surface. Notice that in the experiments the Pt particles have a size of about 1 nm, i.e. much larger than the nano-clusters used here. In this respect the comparison can only be of qualitative nature. For Pt_3 we adopted the triangular configuration as the most stable structure according to a previous DFT study [47]. In this configuration, two Pt atoms bind to two O_{2c} sites of the TiO_2 (101) surface and the other one is pointing towards the vacuum, Figure S6a. It has been reported that planar Pt_4 is the most stable structure on the TiO_2 (110) surface [51]. Beside this structure, we considered also a tetrahedral initial geometry. It turns out that tetrahedral Pt_4 is 0.5 eV more stable than the planar one. In tetrahedral Pt_4 on a-TiO_2 (101) three Pt atoms interact with three O_{2c} sites of TiO_2 and the fourth Pt atom forms the corner of the tetrahedron, Figure S6b.

Table 4. Formal Pt oxidation state, adsorption energy (E_{ads}, eV), C-O bond length (R_{CO}, Å), C-Pt distance (R_{CPt}, Å), Bader charge of Pt bound to CO (Q |e|), scaled harmonic CO stretching frequency (ω_e, cm^{-1}) and frequency shift with respect to the gas-phase (cm^{-1}) for CO adsorption on Pt metal clusters on a-TiO_2 (101) surface.

System	CO site	E_{ads} (eV)	R_{CO} (Å)	R_{CPt} (Å)	Q (|e|)	ω_e (cm^{-1})[a]	$\Delta\omega_e$ (cm^{-1})
$Pt_3(TiO_2)_{60}$	Pt^0-top	1.82	1.165	1.847	0.00	2018	-125
$Pt_3(TiO_2)_{60}$	Pt^0-bottom	2.33	1.161	1.843	+0.33	2052	-91
$Pt_4(TiO_2)_{60}$	Pt^0-top	2.02	1.161	1.846	+0.38	2047	-96
$Pt_4(TiO_2)_{60}$	Pt^0-bottom	2.04	1.163	1.872	+0.08	2030	-113

The properties of CO adsorption on Pt_{metal} clusters are reported in Table 4. Due to the symmetry of Pt atoms in Pt_3 and Pt_4 clusters, two Pt sites were considered for CO adsorption, the Pt top, toward to the vacuum, and Pt bottom, at the interface with TiO_2. These structures are shown in Figure 5. On Pt_3, a large adsorption energy was observed, 1.82 eV for CO bound to Pt top and 2.33 eV for Pt bottom, respectively. On contrary, on Pt_4 the CO adsorption energy, about 2 eV, is independent of

the Pt sites when CO is bound. The Pt-CO bond lengths are also nearly the same. These results are in line with previous DFT studies of CO adsorption on metal Pt surfaces [52,53]. Furthermore, large red-shifts of the CO stretching frequencies are found on Pt_3 and Pt_4, in the range of -91/-125 cm^{-1} which is consistent with experimental FTIR data, Table 1. These results also agree well with the measured CO adsorption energies for the most undercoordinated Pt sites (ie. those where CO has the lowest vibrational frequency). In these calculations it was not possible to relate Pt coordination number in the clusters to CO adsorption energy or vibrational frequency, as done in the experiments, due to the small cluster sizes.

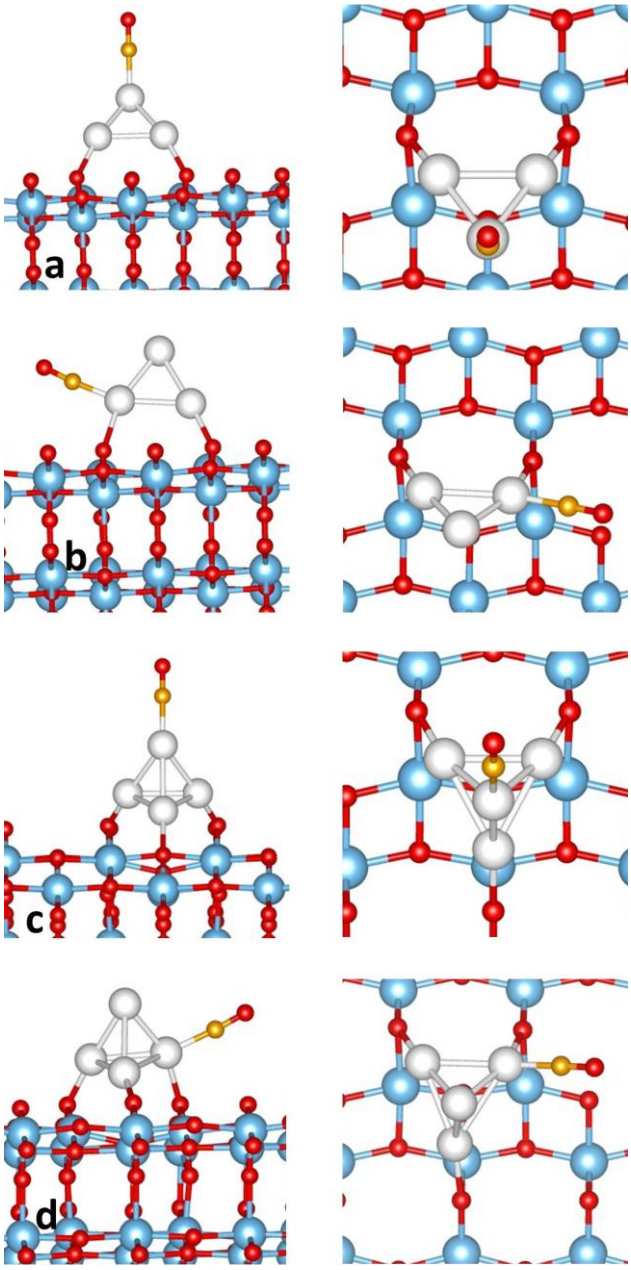

Figure 5. CO adsorption on Pt atom on top site (a), bottom (interface) site (b) of Pt_3 cluster on a-TiO_2 (101) surface and on Pt atom on top site (c), bottom (interface) site (d) of Pt_4 cluster on a-TiO_2 (101) surface with side view (left) and top view (right). Ti, O, Pt and C atoms are blue, red, white and gold spheres, respectively.

3.2.4 Oxidized Pt clusters, Pt_{ox} on a-TiO_2 (101) surface

The experiments show that CO adsorption on oxidized Pt clusters containing cationic Pt (with adsorption energies of 1.72-2.10 eV, Table 1) is a bit stronger than on metallic Pt clusters (1.16-1.93 eV, Table 1). This could be related to the fact that CO interacts with oxidized low-coordinated Pt atoms in Pt_{ox} particles. Therefore, we considered a few Pt_xO_y cluster models with Pt in different oxidation states. As no structural information exists, these structures can be considered as highly hypothetical. Furthermore, the size of the oxidized clusters considered is considerably smaller than that of the Pt_{ox} species (1 nm). We considered Pt_2O_4, Pt_3O_6, Pt_4O_6, and Pt_4O_7 clusters on the a-TiO_2 (101) surface. Assigning a formal oxidation state to the Pt atoms of the adsorbed Pt_{ox} species is not easy, due to the interaction of the clusters with the surface and to the fact that the Pt atoms have different coordination numbers. For this reason, the assigned oxidation states must be taken with care, being more the signature of a different chemical environment of the Pt atom rather than a real assessment of its charge. We also remind that all the systems considered are charge neutral. The first structure, Pt_2O_4 is symmetric with each Pt coordinated to four oxygen atoms, one of which is an O_{2c} of a-TiO_2 (101), Figure S7a. We assigned an oxidation state +III to this Pt, in analogy with our study of Ru atom adsorbed on ZrO_2 [22], since the Pt atoms are involved in a bonding with a O_{2c} anion. In the second model, Pt_3O_6 cluster, the structure can exist with different configurations but we adopted the most stable gas-phase configuration [54], Figure S7b. This model contains two types of Pt atoms; we attributed formal oxidation states +III and +IV, depending on the number of oxygen atoms bound to Pt; the third model consists of two types of Pt with different oxidation states +II, +III, Figure S7c, and the last one contains three different Pt cations with oxidation states +II, +III and +IV, Figure S7d.

Table 5. Formal Pt oxidation state, adsorption energy (E_{ads}, eV), C-O bond length (R_{CO}, Å), C-Pt distance (R_{CPt}, Å), Bader charge of Pt bound to CO (Q |e|), scaled harmonic CO stretching frequency (ω_e, cm^{-1}) and frequency shift with respect to the gas-phase (cm^{-1}) for CO adsorption on Pt oxide clusters on a-TiO_2 (101) surface.

System	CO	E_{ads}	R_{CO}	R_{CPt}	Q (|e|)	ω_e	$\Delta\omega_e$

	site	(eV)	(Å)	(Å)		(cm^{-1})[a]	(cm^{-1})
$Pt_2O_4(TiO_2)_{60}$	Pt^{III}	1.17	1.153	1.850	+1.24	2102	-41
$Pt_3O_6(TiO_2)_{60}$	Pt^{III}	1.62	1.150	1.881	+1.18	2115	-28
$Pt_3O_6(TiO_2)_{60}$	Pt^{IV}	1.82	1.154	1.858	+0.98	2097	-46
$Pt_4O_6(TiO_2)_{60}$	Pt^{II}	2.07	1.158	1.807	+1.00	2086	-57
$Pt_4O_6(TiO_2)_{60}$	Pt^{III}	1.47	1.151	1.891	+0.69	2103	-40
$Pt_4O_7(TiO_2)_{60}$	Pt^{II}	2.29	1.152	1.861	+1.11	2104	-39

For the CO adsorption complexes, we considered all possible adsorption sites on Pt_{ox} clusters deposited on TiO_2 (101), see Table 5 and Figure 6. On Pt_2O_4, the CO adsorption energy, 1.17 eV, is similar as for CO on PtO_2, 1.07 eV. This is consistent with the high oxidation state of Pt (Bader charge, +1.24 |e|). There is a small red-shift of the CO frequency with respect to free CO, -41 cm^{-1}. On Pt_3O_6, two Pt sites with oxidation state +III and +IV were considered. The bonding of CO on Pt(+IV) is stronger than on Pt(+III), 1.82 eV vs. 1.62 eV, respectively. While the Pt atom remains coordinated to three oxygen atoms after CO adsorption for the Pt(+III) case, Figure 6b, the coordination (and oxidation state) of Pt are reduced when CO binds to Pt(+IV), Figure 6c. Although CO adsorption on Pt_2O_4 and Pt_3O_6 models show a similarity to the experimental data in terms of red shift (-28/-46 cm^{-1} vs. -3/-53 cm^{-1}), the smaller CO adsorption energy on Pt_2O_4 and Pt_3O_6 cluster compared to metallic Pt cluster, is not in line with the experimental observation. In this respect, the Pt_xO_{2x} models do not reproduce all the observations.

Thus, we considered other models where the O:Pt ratio is smaller. On Pt_4O_6 cluster, we considered CO adsorption on two Pt atoms, Pt (+III), Pt (+II), Figure 6d and 6e, respectively. As expected, a stronger adsorption energies is found for CO on Pt with the lower oxidation state (+II), 2.02 eV, compared to the Pt with higher oxidation state (+III), 1.47 eV. These adsorption energies are comparable to those measured for cationic Pt, from 1.72 to 2.10 eV, Table 1. The CO vibrational shift, -57 and -40 cm^{-1}, respectively, is also not far from the measured shifts for CO on cationic Pt (-26 to -38 cm^{-1}).

The last model studied is CO adsorption on Pt_4O_7. Also in this case we considered two Pt sites with different oxidation states, Pt (+IV) and Pt (+II). On Pt (+IV), however, CO binds to the extra oxygen to form CO_2, indicating an unstable structure. Therefore we reported only the complex where CO is bound to Pt (+II), Table 5 and Figure 6f. Here a high adsorption energy, 2.29 eV, and small red-shift of CO stretching frequency, -39 cm^{-1}, are obtained. Both E_{ads} and $\Delta\omega_e$ are in

reasonable agreement with the experimental observations. Therefore, we can close this section with the conclusion that the Pt_{ox} clusters should have a stoichiometry not far from $Pt_xO_{1.5x}$.

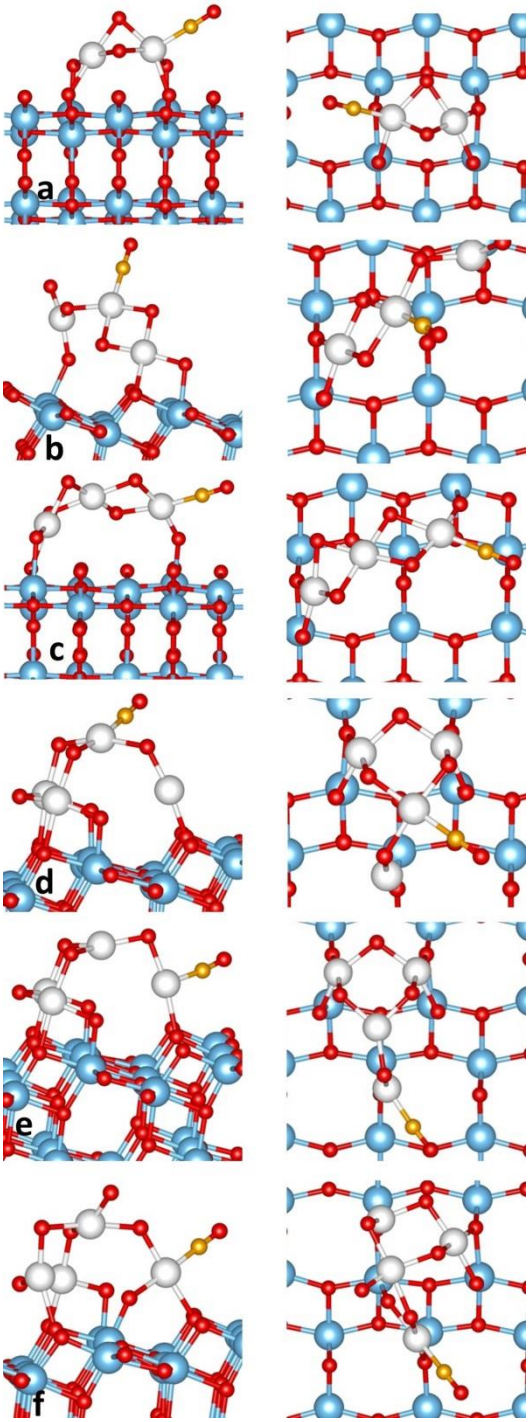

Figure 6. CO adsorption on a) Pt_2O_4, b) Pt_3O_6 at Pt (+IV), c) Pt_3O_6 at Pt (+III), d) Pt_4O_6 at Pt (+III), e) Pt_4O_6 at Pt (+II) and f) Pt_4O_7 at Pt (+II) on a-TiO_2 (101) surface with side view (left) and top view (right). Ti, O, Pt and C atoms are blue, red, white and gold spheres, respectively.

4. Conclusions

Recent experimental studies have reported catalysts consisting of thermally stable Pt atoms, and sub-nanometer sized metallic and oxidized Pt clusters on 5 nm particles of anatase TiO_2. The species have been studied by means of STEM and CO probe molecule FTIR methods, and have been classified as isolated Pt (Pt_{iso}), Pt nanoparticles (Pt_{metal}), and oxidized Pt nanoparticles (Pt_{ox}). The Pt_{iso}/TiO_2 catalysts are active in CO oxidation and show behavior consist with single site cationic Pt species that coordinate to CO more weakly than the Pt_{metal} or Pt_{ox} species. In this work, the characterization has been extended by performing an analysis of the FTIR spectral features of the various species in combination with new TPD data. This allows us to obtain estimates of the CO vibrational properties and adsorption energies to be compared with extensive DFT+U calculations.

The FTIR analysis of CO adsorption on these species show a symmetric, narrow and unchanged band at 2113 cm^{-1} due to atomically dispersed Pt atoms; a broader set of band at 2028-2079 cm^{-1} attributed to Pt_{metal} particles; and bands in the range 2105-2117 cm^{-1} attributed to cationic Pt species in Pt_{ox} nanoparticles. The corresponding CO adsorption energies are: Pt_{iso} 0.87 eV; Pt_{metal} 1.16-1.93 eV; cationic sites of Pt_{ox} 1.72-2.10 eV.

Various models of single Pt atoms, metallic Pt clusters and oxidized Pt clusters adsorbed on a-TiO_2 (101) and a-TiO_2 (145) surfaces have been considered. By comparison between calculated results and experimental data, some conclusions can be drawn:

- In agreement with our previous study on Ru adsorbed on ZrO_2 [22], a large redshift is found for the frequencies of CO adsorbed on atomic Pt on TiO_2 (101) surface as compared to gas phase CO, despite the positive oxidation state of the metal atom. This is due to the presence of a sufficient electron density on the 5d levels of Pt, which also suggests a potential catalytic role of this species.
- A single Pt atom incorporated into TiO_2 by replacing a Ti or an O atom in the lattice, suggested experimentally to explain the strong thermal stability of Pt atoms on rutile TiO_2 [50], is incompatible with the computed data. In fact, neither the CO adsorption energy nor the CO ω shift for $(Pt)_{subTi5c}$ or $(Pt)_{subO2c}$ match the experimental results.
- Oxidized Pt clusters with stochiometries close to $Pt_xO_{1.5x}$ result in high CO adsorption energies, and moderate vibrational frequency redshifts, consistent with the experimental measurements on Pt_{ox} clusters. Small metallic Pt clusters exhibit large red shifts and CO binding energies comparable and in some cases smaller that $Pt_xO_{1.5x}$ clusters. Both the small metallic and $Pt_xO_{1.5x}$ clusters exhibit much stronger CO binding as compared to $(PtO_2)_{ads.}$ These trends are all in good agreement with the experimental results.

- It is interesting to consider that CO on the $Pt_xO_{1.5x}$ and $(PtO_2)_{ads}$ structures give similar CO vibrational frequencies, but almost 1 eV difference in binding energy. This is due primarily to the more flexible structure of $Pt_xO_{1.5x}$ species compared to the rigid $(PtO_2)_{ads}$, which does not significantly change structure to accommodate strong CO binding.
- The moderate redshifts (-41/-22 cm^{-1}) of CO bound to $(PtO)_{ads}$ and $(PtO_2)_{ads}$ species are in line with the experimental observation (-33 cm^{-1}). However, a strong adsorption energy and an important restructuring are found when CO is bound to $(PtO)_{ads}$, indicating that this species in incompatible with the experimental Pt_{iso} species. On the other hand, an excellent agreement with experiment in both CO frequencies and adsorption energies is found for $(PtO_2)_{ads}$ models. In particular, a $(PtO_2)_{ads}$ adsorbed on the terraces of the TiO_2 (101) surface exhibits a CO ω_e of 2121 cm^{-1} (exp. 2113 cm^{-1}) and an adsorption energy of 1.07 eV (exp. 0.87 eV). Notice that in these models Pt is bound to three O atoms, giving rise to a strongly trapped species, and that Pt is just above a Ti atom of the lattice, making its identification possible in TEM measurements.

It is worth discussing the findings here in the context of recent reports that relied on CO probe molecule IR spectroscopy as a primary means to characterize Pt_{iso} species [55,56,57,58]. Here it was shown that Pt_{iso} species in different adsorption sites on TiO_2 display a range of characteristics (ω and E_{ads}) for adsorbed CO, which require detailed comparison to distinguish from CO adsorbed to small Pt clusters. Given the similar characteristics of adsorbed CO on various sub-nanometer Pt species, analyses attempting to relate local structure to function for Pt_{iso} species should ensure that there is no contribution from small Pt clusters, and further that Pt_{iso} species are homogeneously dispersed at similar sites on the support. A recent analysis that achieved this precise characterization showed that Pt_{iso} species on thin Cu oxide films on Cu single crystals are of neutral charge, which results in an adsorbed CO stretch of 2028 cm^{-1}, clearly distinct from the 2113 cm^{-1} stretch reported here [57]. This difference in behavior as a function of support demonstrates the importance of Pt_{iso}-support interactions for the functionality of this class of catalysts.

Acknowledgments

P.C. acknowledges funding from the National Science Foundation (NSF) CAREER grant number CBET-1554112. The work of T. V. H. and G. P. has been supported by the Italian MIUR through the PRIN Project 2015K7FZLH SMARTNESS "Solar driven chemistry: new materials for photo– and electro–catalysis".

References

[1] E.C. Tyo, S. Vajda, Catalysis by clusters with precise numbers of atoms, Nature Nanotechnology 10 (2015) 577–588.

[2] F. Calaza, C. Stiehler, Y. Fujimori, M. Sterrer, S. Beeg, M. Ruiz-Oses, N. Nilius, M. Heyde, T. Parviainen, K. Honkala, H. Hakkinen, H.-J. Freund, Carbon dioxide activation and reaction induced by electron transfer at an oxide–metal interface, Angew. Chem. Int. Ed. 54 (2015) 12484 –12487.

[3] A.R. Puigdollers, P. Schlexer, S. Tosoni, G. Pacchioni, Increasing oxide reducibility: The role of metal/oxide interfaces in the formation of oxygen vacancies, ACS Catal. 7 (2017) 6493–6513.

[4] M.M. Khader, M.J. Al-Marri, S. Ali, A.G. Abdelmoneim, Active and stable methane oxidation nano-catalyst with highly-ionized palladium species prepared by solution combustion synthesis, Catalysts 8 (2018) 66.

[5] B.E. Hayden, D. Pletcher, M E. Rendall, J.P. Suchsland, CO oxidation on gold in acidic environments: Particle size and substrate effects, J. Phys. Chem. C 111 (2007) 17044-17051.

[6] T. Risse, S. Shaikhutdinov, N. Nilius, M. Sterrer, H.-J. Freund, Gold supported on thin oxide films: From single atoms to nanoparticles, Acc. Chem. Res. 42 (2008) 949-956.

[7] S. Tosoni, G. Pacchioni, Influence of surface hydroxylation on the Ru atom diffusion on the ZrO_2(101) surface: A DFT study, Surf. Sci. 664 (2017) 87-94.

[8] B. Qiao, A. Wang, X. Yang, L. F. Allard, Z. Jiang, Y. Cui, J. Liu, J. Li, T. Zhang, Single-atom catalysis of CO oxidation using Pt_1/FeO_x. Nat. Chem. 3 (2011) 634-641.

[9**]** Y. Lou, J. Liu, CO oxidation on metal oxide supported single Pt atoms: The role of the support, Ind. Eng. Chem. Res. 56 (2017) 6916–6925.

[10] S. Sun, G. Zhang, N. Gauquelin, N. Chen, J. Zhou, S. Yang, W. Chen, X. Meng, D. Geng, M. N. Banis, R. Li, S. Ye, S. Knights, G. A. Botton, T.-K. Sham, X. Sun, Single-atom catalysis using Pt/graphene achieved through atomic layer deposition, Sci. Rep.3 (2013) 1775.

[11] T. Imaoka, Y. Akanuma, N. Haruta, S. Tsuchiya, K. Ishihara, T. Okayasu,W.-J. Chun, M. Takahashi, K. Yamamoto, Platinum clusters with precise numbers of atoms for preparative-scale catalysis. Nat. Comm. 8 (2017) 688.

[12] O. Mathieu, J. Lavy, E. Jeudy, Investigation of hydrocarbons conversion over a Pt-based automotive diesel oxidation catalyst: application to exhaust port fuel injection, Top. Catal. 52 (2009) 1893–1897.

[13] H. Hoshi, S. Tanaka, T. Miyoshi, Pt-graphene electrodes for dye-sensitized solar cells, Materials Science and Engineering B 190 (2014) 47–51.

[14] S.-S. Kim, K.-W. Park, J.-H. Yum, Y.-E. Sung, Dye-sensitized solar cells with Pt–NiO and Pt–TiO_2 biphase counter electrodes, Journal of Photochemistry and Photobiology A: Chemistry, 189 (2007) 301–306.

[15] J. Jones, H. Xiong, A.T. DeLaRiva, E.J. Peterson, H. Pham, S.R. Challa, G. Qi, S. Oh, M.H. Wiebenga, X.I. P. Hernández, Y. Wang, A. K. Datye, Thermally stable single-atom platinum-on-ceria catalyst via atom trapping, Science 353 (2016**)** 150-154.

[16] Z. Zhang, Y. Zhu, H. Asakura, B. Zhang, J. Zhang, M. Zhou, Y. Han, T. Tanaka, A. Wang, T. Zhang, N. Yan, Thermally stable single atom Pt/m-$Al_2O_3$for selective hydrogenation and CO oxidation, Nat. Comm. 8 (2017) 16100.

[17] A. Bruix, Y. Lykhach, I. Matolnova, A. Neitzel, T. Skla, N. Tsud, M. Vorokhta, V. Stetsovych, K. Sevckov, J. Myslivecek, R. Fiala, M. Vclavu, K. C. Prince, S. Bruyre, V. Potin, F. Illas, V. Matoln, J. Libuda, K. M. Neyman, Maximum noble-metal efficiency in catalytic materials: atomically dispersed surface platinum, Angew. Chem., int. Ed. 53 (2014**)** 10525.

[18 **]** J.H. Kwak, J. Hu, D. Mei, C.-W. Yi, D.H. Kim, C.H. Peden, L.F. Allard, J. Szanyi, Coordinatively unsaturated Al^{3+} centers as binding sites for active catalyst phases of platinum on gamma-Al_2O_3. Science 325 (2009) 1670-1673.

[19] B. Zhang, H. Asakura, J. Zhang, J. Zhang, S. De, N. Yan, Stabilizing a $platinum_1$ single-atom catalyst on supported phosphomolybdic acid without compromising hydrogenation activity, Angew. Chem. Int. Ed. 55 (2016) 8319 –8323.

[20] L. DeRita, S. Dai, K Lopz-Zepda, N. Pham, G.W. Graham, X. Pan, P. Christopher, Catalyst architecture for stable single atom dispersion enables site-specific spectroscopic and reactivity measurements of CO adsorbed to Pt atoms, oxidized Pt clusters, and metallic Pt clusters on TiO_2, J. Am. Chem. Soc. 139 (2017) 14150-14165.

[21] H.A. Aleksandrov, K.M. Neyman, K.I. Hadjiivanov and G.N. Vayssilov, Can the state of platinum species be unambiguously determined by the stretching frequency of an adsorbed CO probe molecule?, Phys. Chem. Chem. Phys.18 (2016) 22108-22121.

[22 V.T. Ho, S. Tosoni, G. Pacchioni, L. Fang, P. Bruijnincx, Nature of sintering-resistant, single-atom Ru species dispersed on zirconia-based catalysts. A DFT and FTIR study of CO adsorption, ChemCatChem 10 (2018) 1-3.

[23] H. Sellers, Entropies of desorption from temperature programmed desorption data: Trends and applications to rate constant determinations, J. Phys. Chem. B 107 (2003) 10206–10208.

[24] C.T. Campbell, J.R.V. Sellers, Enthalpies and entropies of adsorption on well-defined oxide surfaces: Experimental measurements, Chem. Rev.113 (2013) 4106–4135.

[25] P.A. Redhead, Thermal desorption of gases, Vacuum 12. (1962) 203-211.

[26] G. Kresse, J. Furthmüller, Efficiency of ab-initio total energy calculations for metals and semiconductors using a plane-wave basis set, J. Comput. Mater. Sci. 6 (1996) 15-50.

[27] J. P. Perdew, K. Burke, M. Ernzerhof, Generalized gradient approximation made simple, Phys. Rev. Lett. 77 (1996) 3865-3868.

[28] H.Y.T. Chen, S. Tosoni, G. Pacchioni, Adsorption of ruthenium atoms and clusters on anatase TiO_2 and tetragonal ZrO_2 surfaces: A comparative DFT study. J. Phys. Chem. C 119 (2015) 10856-10868.

[29] P.E. Blöchl, Projector augmented-wave method, Phys. Rev. B 50 (1994) 17953.

[30] G. Kresse, J. Joubert, From ultrasoft pseudopotentials to the projector augmented-wave method, Phys. Rev. B 59 (1999) 1758.

[31] H. Y. T. Chen, S. Tosoni, G. Pacchioni, A DFT study of the acid-base properties of anatase TiO_2 and tetragonal ZrO_2 by adsorption of CO and CO_2 probe molecules, Surf. Sci. 652 (2016) 163–171.

[32] W. Tang, E. Sanville, G. Henkelman, A grid-based bader analysis algorithm without lattice bias, J. Phys.: Condens. Matter. 21 (2009) 084204.

[33] E. Sanville, S. D. Kenny, R. Smith, G. Henkelman, An improved grid-based algorithm for bader charge allocation. J. Comp. Chem. 28 (2007) 899-908.

[34] G. Henkelman, A. Arnaldsson, H. Jónsson, A fast and robust algorithm for bader decomposition of charge density, Comput. Mater. Sci. 36 (2006) 254-360.

[35] M. Yu, D. R. Trinkle, Accurate and efficient algorithm for bader charge integration, J. Chem. Phys. 134 (2011) 064111.

[36] B. Qiao, A. Wang, X. Yang, L.F. Allard, Z. Jiang, Y. Cui, J. Liu, Single-atom catalysis of CO oxidation using Pt_1/FeO_x, Nat. Chem. 3 (2011) 634-641.

[37] K. Ding, A. Gulec, A.M. Johnson, N.M. Schweitzer, G.D. Stucky, L.D. Marks, P.C. Stair, Identification of active sites in CO oxidation and water-gas shift over supported Pt catalysts, Science. 350 (2015) 189-192.

[38] A. Crossley, D.A King, Infrared spectra for CO isotopes chemisorbed on Pt “111”: Evidence for strong adsorbate coupling interactions, Surf. Sci. 68 (1977) 528-538.

[39] M.J. Kappers, J.H. van der Maas, Correlation between CO frequency and Pt coordination number. A DRIFT study on supported Pt catalysts, Catalysis Letters 10 (1991) 365-373.

[40] M.J. Kale, P. Christopher, Utilizing quantitative in situ FTIR spectroscopy to identify well-coordinated Pt atoms as the active site for CO oxidation on Al2O3-supported Pt catalysts, ACS Catal. 6 (2016) 5599-5609.

[41] F.M. Leibsle, R.S. Sorbello, R.G. Greenler, Coupled harmonic oscillator models of carbon monoxide adsorbed on stepped, platinum surfaces, Surf. Sci. 179 (1987) 101-118.

[42] T. Avanesian, S. Dai, M.J. Kale, G.W. Graham, X. Pan, P. Christopher, Quantitative and atomic-scale view of CO-induced Pt nanoparticle surface reconstruction at saturation coverage via DFT calculations coupled with in Situ TEM and IR, J. Am. Chem. Soc. 139 (2017) 4551-4558.

[43] B.E. Hayden, K. Kretzschmar, A.M. Bradshaw, R.G Greenler, An infrared study of the adsorption of CO on stepped platinum surface, Surf. Sci. 149(1985) 394-406.

[44] M.J. Lundwall, S.M. McClure, D.W Goodman, Probing terrace and step sites on Pt nanoparticles using CO and ethylene, J. Phys. Chem. C 114 (2010) 7904-7912.

[45] M. Primet, J.M. Basset, M.V. Mathieu, M. Prettre, Infrared study of CO adsorbed on $PtAl_2O_3$. A method for determining metal-adsorbate interactions, J. Catal. 29 (1973) 213-223.

[46] C. Asokan, L. DeRita, P. Christoper, Using probe molecule FTIR spectroscopy to identify and characterize Pt-group metal based single atom catalysts, Chinese Journal of Catalysis 38 (2017) 1473-1480.

[47] Y. Han, C.-j. Liu, Q. Ge, Interaction of Pt clusters with the anatase TiO_2 (101) surface: A first principles study, J. Phys. Chem. B 110 (2006) 7463-7472.

[48] Y. Zhou, C.L. Muhich, B.T. Neltner, A.W. Weimer, C. B. Musgrave, Grouth of Pt particles on the anatase TiO_2 (101) surface, J. Phys. Chem. C 116 (2012) 12114-12123.

[49] A.S. Hoffman, C.-Y. Fang, B.C. Gates, Homogeneity of surface sites in supported single site metal catalysts: Assessment with band widths of metal carbonyl infrared spectra, J. Phys. Chem. Lett. 7 (2016) 3854–3860.

[50] T.-Y. Chang, Y. Tanaka, R. Ishikawa, K. Toyoura, K. Matsunaga, Y. Ikuhara, N. Shibata, Direct imaging of Pt single atoms adsorbed on TiO_2 (110) surfaces, Nano Lett. 14 (2014) 134-138.

[51] A.S. Maldonado, C.I.N. Morgade, S.B. Ramos, G.F. Cabeza, Comparative study of CO adsorption on planar and tetragonal Pt nanoclusters supported on TiO_2(110) stoichiometric and reduced surfaces, Molecular Catalysis 433 (2017) 403-413.

[52] S. Yamagishi, T. Fujimoto, Y. Inada, H. Orita, Studies of CO adsorption on Pt(100), Pt(410), and Pt(110) surfaces using density functional theory, J. Phys. Chem. B 109 (2005) 8899-8908.

[53] H. Orita, Y. Inada, DFT investigation of CO adsorption on Pt(211) and Pt(311) surfaces from low to high coverage, J. Phys. Chem. B 109 (2005) 22469-22475.

[54] Y. Xu, W.A. Shelton, W.F. Schneider, Thermodynamic equilibrium compositions, structures, and reaction energies of Pt_xO_y (x = 1-3) clusters predicted from first principles, J. Phys. Chem. B 110 (2006) 16591-16599.

[55] K. Ding, A. Gulec, A.M. Johnson, N. M. Schweitzer, G. D. Stucky, L. D. Marks, P.C. Stair, Identification of active sites in CO oxidation and water-gas shift over supported Pt catalysts, Science 350 (2015) 189–192.

[56] L. Nie, D. Mei, H. Xiong, B. Peng, Z. Ren, Z.I.P. Hernansez, A. DeLaRiva, M. Wang, M.H. Engelhard, L. Kovarik, A.K. Datye, Y. Wang, Activation of surface lattice oxygen in single-atom Pt/CeO_2 for low-temperature CO oxidation, Science 358 (2017) 1419–1423.

[57] A.J. Therrien, A.J.R Hensley, M.D. Marcinkowski, R. Zhang, F.R. Lucci, B. Coughlin, A.C. Schilling, J.-S. McEwen, E.C.H. Sykes, An atomic-scale view of single-site Pt catalysis for low-temperature CO oxidation, Nat. Catal. 1 (2018) 192-198.

[58] J. Liu, F.R. Lucci, M. Yang, S. Lee, M.D. Marcinkowski, A.j. Therrien, C.T. Williams, E.C.H. Sykes, M. Flutzani-Stephanopoulos, Tackling CO Poisoning with Single-Atom Alloy Catalysts, J. Am. Chem. Soc. 138 (2016) 6396–6399.

Table of Content Graphic